Materials Horizons

Direct Ink Writing of Organic and Carbon Aerogels

Journal:	*Materials Horizons*
Manuscript ID	MH-COM-05-2018-000603.R2
Article Type:	Communication
Date Submitted by the Author:	20-Aug-2018
Complete List of Authors:	Chandrasekaran, Swetha; Lawrence Livermore National Security LLC, Yao, Bin; University of California, Santa Cruz, Chemistry and biochemistry Liu, Tianyu; Virginia Polytechnic Institute and State University, Department of Chemistry Xiao, Wang; University of California, Santa Cruz, Chemistry and biochemistry Song, Yu; Northeastern University, Department of Chemistry Qian, Fang; Lawrence Livermore National Lab, Zhu, Cheng; Lawrence Livermore National Laboratory Duoss, Eric; Lawrence Livermore National Laboratory, Physical and Life Sciences Spadaccini, Christopher; Lawrence Livermore National Laboratory, Center for Micro and Nano Technology Li, Yat; University of California, Department of Chemistry and Biochemistry Worsley, Marcus; Lawrence Livermore National Laboratory, Physical and Life Sciences Directorate

Direct Ink Writing of Organic and Carbon Aerogels

Swetha Chandrasekaran[‡a], Bin Yao[‡b], Tianyu Liu[b], Wang Xiao[b], Yu Song[b], Fang Qian[a], Cheng Zhu[c], Eric B. Duoss[c], Christopher M. Spadaccini[c], Yat Li[*b], Marcus A. Worsley[*a]

Conceptual Insight

This study reports unique electrochemical phenomenon in carbon aerogels and proposes new guidelines to electrode design. The use additive manufacturing (e.g. 3D printing) to control the feature and pore size in aerogel electrodes facilitates rapid ion transport in the electrode, significantly improving the capacitance at high charge/discharge rates. Compared with bulk aerogel electrodes with primarily sub-micron pores that severely limit transport, the 3D printed aerogels enable much faster ion diffusion kinetics and provide an unprecedented rate capability for millimeter aerogel electrodes. Further enhancements are realized by printing finer aerogel features (reducing diffusion lengths) and increasing the aerogel surface area to almost 2000 m^2/g, which is unprecedented for 3D printed aerogels reported to date. This work highlights the benefits of 3D printing aerogel materials via sol-gel chemistry in order to overcome the limitations inherent to this class of materials.

---

[a] *Physics and Life Science Directorate, Lawrence Livermore National Laboratory, Livermore, California 94550, United States.*
[b] *Department of Chemistry and Biochemistry, University of California, Santa Cruz, California 95064, United States.*
[c] *Engineering Directorate, Lawrence Livermore National Laboratory, Livermore, California 94550, United States.*
‡ These authors contributed equally to this work.
* Corresponding authors: yatli@ucsc.edu, worsley1@llnl.gov

Direct Ink Writing of Organic and Carbon Aerogels

Swetha Chandrasekaran[1‡], Bin Yao[2‡], Tianyu Liu[2], Wang Xiao[2], Yu Song[2], Fang Qian[1], Cheng Zhu[3], Eric B. Duoss[3], Christopher M. Spadaccini[3], Yat Li[2]*, Marcus A. Worsley[1]*

[1] Physics and Life Science Directorate, Lawrence Livermore National Laboratory, Livermore, California 94550, United States.
[2] Department of Chemistry and Biochemistry, University of California, Santa Cruz, California 95064, United States.
[3] Engineering Directorate, Lawrence Livermore National Laboratory, Livermore, California 94550, United States.

‡ These authors contributed equally to this work.

** Corresponding authors: yatli@ucsc.edu, worsley1@llnl.gov*

Abstract

The use of additive manufacturing to 3D print aerogels has the potential to impact several important technologies such as energy storage, catalysis, and desalination. While there has been a great deal of focus on graphene aerogels, reports of 3D printed conventional carbon aerogels (CAs) are sparse. Activated CAs are particularly compelling because in addition to having a lower cost than a comparable graphene aerogel, they can achieve much higher surface areas (>3000 m^2/g). Herein we report a 3D printable ink based on traditional resorcinol-formaldehyde sol-gel chemistry that can produce a final activated carbon aerogel with surface areas approaching 2000 m^2/g and good electrical conductivities (~200 S/m). Direct ink writing (DIW) is used to then fabricate electrodes, which demonstrate excellent electrochemical properties with a high specific capacitance of 215 F/g at 1 A/g and 83% capacitive retention at higher current densities (10 A/g). The DIW electrode significantly outperformed its bulk counterpart and provides an example of how one can use 3D printed aerogel electrodes to overcome mass transport limitations and boost energy storage performance.

Graphical Abstract

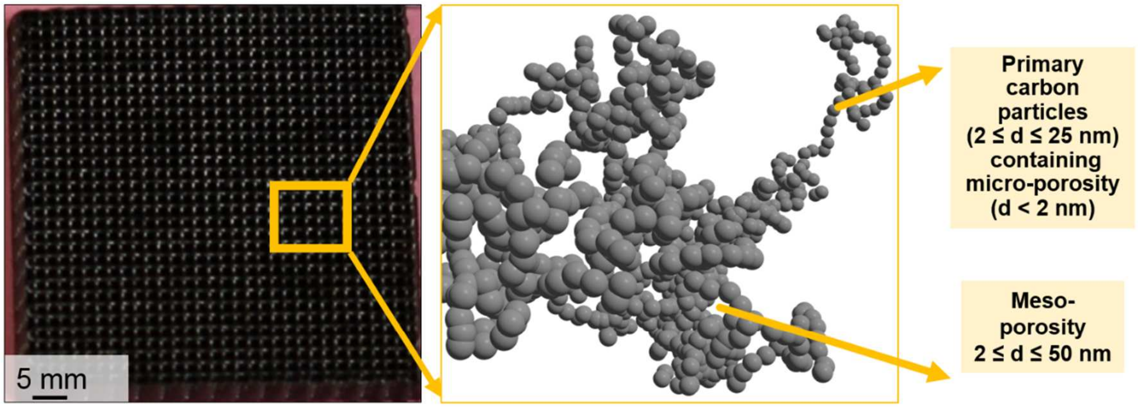

Carbon aerogels (CAs) are unique porous solids with network structures consisting of interconnected carbon particles and, as a result, these materials exhibit many interesting properties, such as high surface-to-volume ratios, continuous porosities and high electrical conductivity [1]. These porous aerogels are currently used in a variety of applications which include catalysis, energy storage, and sorbents [2–5]. Baumann et al., reported synthesis of ultra-high surface area carbon aerogel monoliths (obtained from resorcinol and formaldehyde) through thermal activation [6]. By controlling the mass loss during thermal activation with CO_2, the formation of micropores (pores with diameters less than 2 nm) yielded carbon aerogels with surface areas as high as 3000 m^2/g [7]. These activated carbon aerogels (ACAs) possessed a unique bimodal porosity where the presence of micropores etched into the walls of micron-sized channels could facilitate ion diffusion and produce large capacitances. Therefore, these ACAs are attractive candidates for electrical energy storage devices (supercapacitors, batteries, etc.) and are currently being developed as electrode materials for desalination via capacitive de-ionization [8, 9].

The use of additive manufacturing to print 3D porous carbons has been primarily demonstrated via micro-extrusion of graphene-based inks or carbonization of 3D-printed polymer resins [10–20]. For energy storage applications, Zhu et al., used direct ink writing (DIW) to 3D print a graphene aerogel electrodes that exhibited enhanced mechanical properties, good electrical conductivities, and surface areas up to 740 m^2/g [17]. Capacitive retention of the 3D printed microlattices was an exceptional 90% from current densities of 0.5 A/g to 10 A/g for thick (ca. 1 mm) electrodes. This extraordinary performance was attributed to the macropore architecture made possible by 3D printing the electrode. Given the modest surface areas (less than 1000 m^2/g) and corresponding capacitance (ca. 70 F/g) of this example, one would expect that a 3D printed ACA with surface areas in excess of 1000 m^2/g should provide a significant boost to electrode performance. Gao et. al., also fabricated graphene oxide aerogels through direct ink writing, and reported their performance for supercapacitor applications [21]. However, to date, there are no reports of 3D printable ACAs. In this study, we report the development of 3D printable acid-catalyzed resorcinol-formaldehyde (RF) organic aerogel. The organic aerogel ink is printed via DIW by extruding the ink through nozzles as small as 100 μm in diameter. The organic aerogels are then converted to electrically conductive 3D printed CAs (DIW-CA) via pyrolysis in nitrogen making them suitable as electrodes. The electrodes (DIW–CA) are then activated using CO_2 to increase the surface area to almost 2000 m^2/g. These high surface area DIW-ACA electrodes exhibit capacitances over 200 F/g, much higher than that of the DIW-CA and previously reported 3D printed electrodes. Furthermore, by changing the ligament diameter of the 3D printed electrodes, a significant improvement in the capacitive retention is observed, revealing the superiority of high resolution 3D printing techniques. This work demonstrates the value of leveraging conventional organic sol-gel methods in 3D printing technologies to overcome some of the traditional limitations of aerogels. Specifically, engineering macroporosity into large surface area DIW-ACA electrodes allows one to simultaneously realize high capacitance and good capacitive retention.

The key challenge to 3D printing conventional organic aerogels is the formulation of a printable ink. In order for an ink to be printable, it needs to possess a thixotropic rheology, i.e. the ink must flow easily under shear (e.g. through the nozzle) yet retain its shape immediately after deposition. The conventional reaction mixture for synthesizing RF gels involves mixing resorcinol (1.23 g, 0.112 mol) and a 37% formaldehyde solution (1.7 g, 0.224 mol) in water (1.5 ml), followed by the addition of glacial acetic acid (0.44 g, 0.007 mol). As shown in Fig. 1a, this RF solution has an unsuitably low viscosity for printing. With the addition of hydroxy propyl methyl cellulose the ink now exhibits a higher viscosity and the required shear-thinning behavior (i.e. viscosity decreases with shear rate). However, with cellulose alone, it lacks the ability to retain its shape after deposition, as evidenced by the low stiffness (i.e. storage modulus) in Fig. 1b. The addition of fumed silica (purchased from Carbosil EH5), increases viscosity and imparts additional stiffness which enhances the printability of the ink. RF inks without silica exhibit a plateau of its storage modulus G′ at 300 Pa. Meanwhile, the addition of 9 wt% silica to the RF-cellulose ink increases the modulus by 2 orders of magnitude. Although there is not a significant difference in the viscosity of the RF inks with and without silica, the storage modulus of the RF ink without silica drops drastically at very low shear stress of 10 Pa. Fig. 1b also shows that the use of cellulose alone results in an ink with a stiffness ($<10^3$ Pa) much lower than that previously reported for GO ink [12].

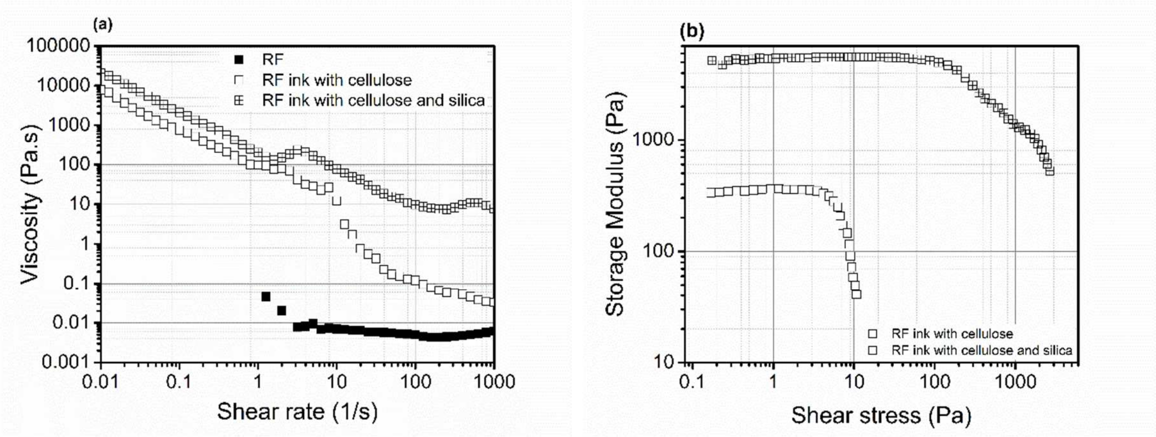

Figure 1: Log-log plots of (a) viscosity as a function of shear rate and (b) storage modulus as a function of shear stress of RF inks.

Fig. 2a, shows the storage modulus of the RF inks measured as a function of time. Since the RF sol-gel process is dynamic with time, it is necessary to monitor the change in the stiffness of the ink over time. Though the RF ink with cellulose alone increases in stiffness with time, its modulus remains orders of magnitude below that required for a printable ink. With the addition of silica, the stiffness and shear yield stress of the inks increase initially and with time, improving printability and suggesting that the silica does not significantly interfere with the sol-gel process. Specifically, with time, the addition of silica increased the storage modulus to 10^5 Pa, consistent is with the previously developed GO inks [12], thereby resulting in a printable RF ink.

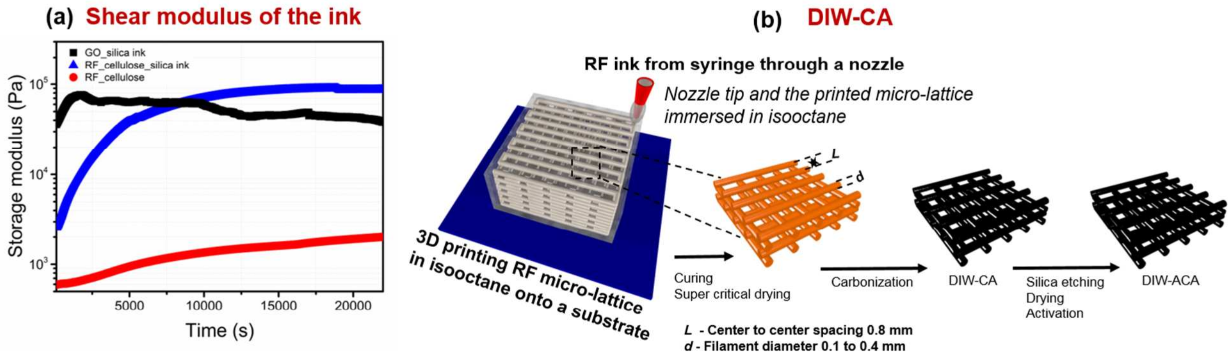
(a) Shear modulus of the ink

(b) DIW-CA

(c) Traditional Carbon Aerogel synthesis

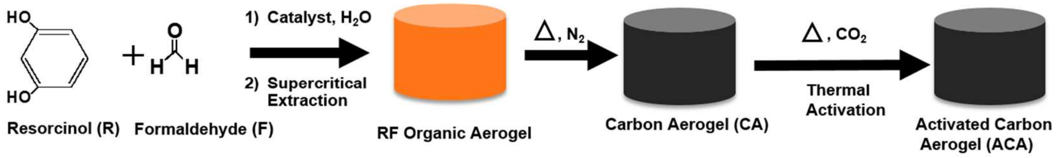

Figure 2: (a) Rheology data of the ink where shear modulus is measured as a function of time, (b) schematic diagram of the DIW printed carbon aerogels and (c) traditional CA synthesis schematic.

After the ink rheology is properly tuned, it is then loaded into a syringe barrel (3 ml or 20 ml in volume). The ink is then centrifuged at 4500 rpm for 2 minutes to remove trapped gas, after which the ink is extruded through a micro nozzle (100-400 μm in diameter at the tip opening) to pattern 3D structures. A schematic of the 3D printing and traditional methods for making the DIW-ACA and ACA, respectively, is shown in Fig. 2b-c. For the DIW-ACA, cubic lattices with multiple orthogonal layers of parallel cylindrical rods are printed alternately. The diameter of the cylindrical rods equals the inner diameter of the nozzle and the center-to-center rod spacing is kept constant at 0.8 mm. The z-spacing during the print is set to 60% of the nozzle diameter and the number of layers stacked on the structure is varied to achieve the desired thickness of the final electrode. To create organic aerogels, the printed structures must remain wet during printing and gelation so that the gels can be dried via supercritical drying to avoid collapse of pores due to capillary forces. Therefore, during printing the part was immersed in an organic solvent (2,2,4-trimethyl-pentane) that is immiscible with the aqueous RF ink.

After printing, the RF parts on the glass substrate are carefully placed in a container with the solvent (2,2,4-trimethyl-pentane) and sealed tightly before being placed in the oven for gelation at 80°C for 72 h. Once gelled, the aqueous solvent is removed by soaking the 3D printed parts in an acetone bath for 3 days with exchange of acetone every 24 h. The samples are then super critically dried using liquid CO_2. To form CAs, the dried 3D printed RF aerogels are subjected to a carbonization step where the samples are heated in a tube furnace under nitrogen atmosphere at 1050 °C for 3 h. These carbonized aerogels are denoted as DIW-CA. After carbonization, the silica particles incorporated in DIW-CAs are etched with hydrofluoric acid similar to the previous work [17]. To activate these aerogels, the samples are heated to 950 °C under CO_2 atmosphere. By tuning the time of exposure of the samples to CO_2, a controlled etching of carbon framework is carried out. This results in the formation of new micropores which in turn increases the surface area. In the present study, the time of exposure was adjusted until a mass loss of nearly 60±2 % was achieved after the activation and the obtained samples are referred to as DIW-ACA.

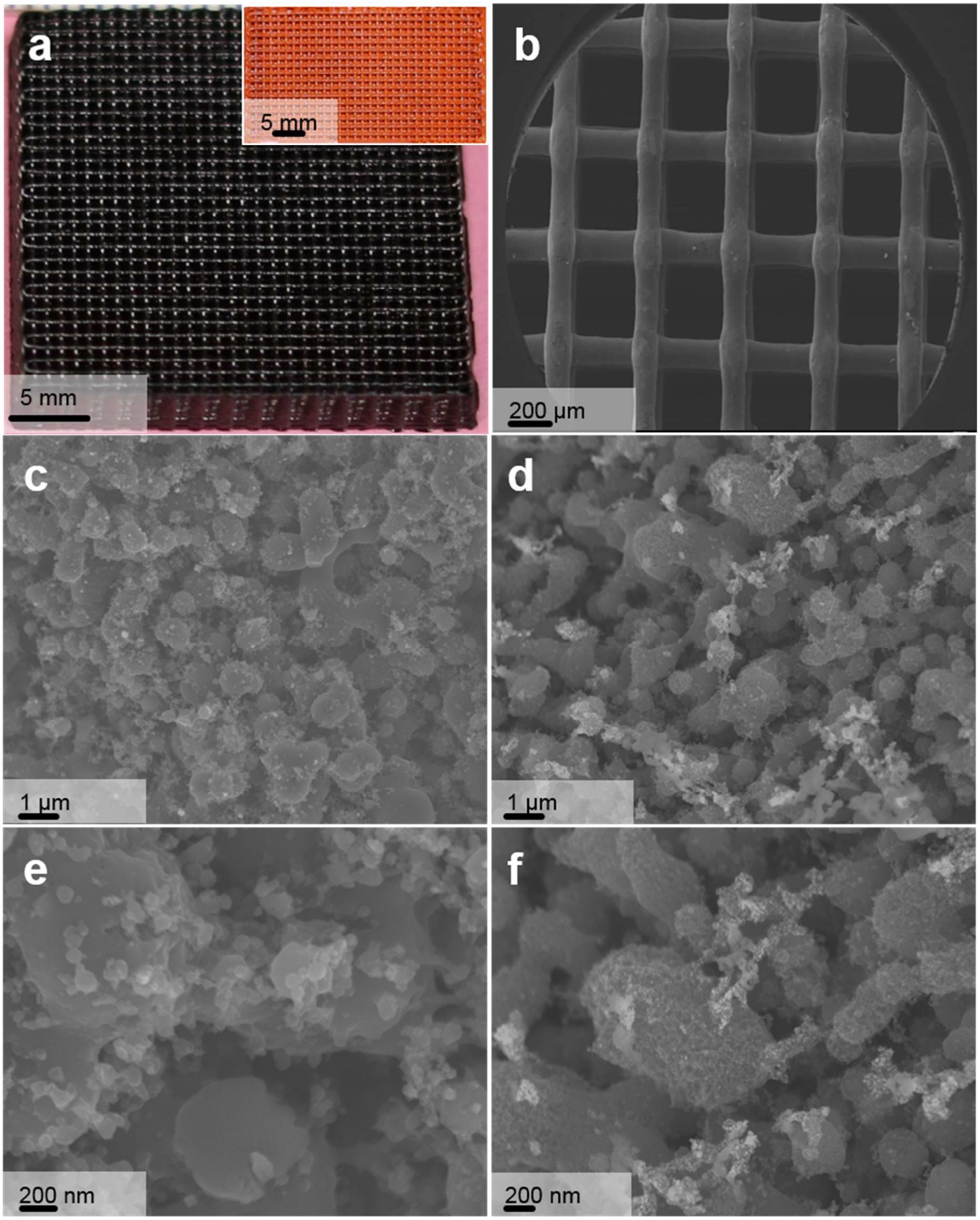

Figure 3: (a) Digital photograph and (b) SEM image of DIW-CA. Magnified SEM images of (c, e) DIW-CA and (d, f) DIW-ACA. Inset in (a) shows 3D-printed organic aerogel before carbonization.

Fig. 3a shows an optical image of a DIW-CA where the inset - an optical image shows the 3D printed RF aerogel before carbonization. The printed DIW-CA lattice maintains its structural integrity through a series of post-processing steps (e.g., solvent exchange, gelation, carbonization, activation). The scanning electron micrograph of the DIW-CA cubic lattice (Fig. 3b) contains parallel cylindrical filaments with multiple orthogonal layers piled on top of each other. Unlike, the GO inks reported earlier [12, 17], during printing, the RF inks are relatively soft and hence the filaments became ellipsoidal at cross-over points in the lattice. These 3D simple cubic lattices are designed with an in-plane center-to-center rod spacing (L) of 0.8 mm and a rod diameter (d) of 0.25 mm, resulting in a spacing-to-diameter ratio (L/d) of ca. 3. The printed sample in Fig. 3a was printed with a print speed of 3 mm/sec, a pressure of 16 psi was applied to extrude the ink from the syringe barrel. For every incremental layer, the nozzle moves up by 0.15 mm or 0.24 mm depending on the nozzle diameter in the z-direction. Note, that the samples undergo a volumetric shrinkage of 21% during gelation, drying and carbonization. Hence, while printing this shrinkage is taken into consideration while setting the dimensions of the sample.

Upon closer examination (Fig. 3c) the morphology of the DIW-CA reveals a network of interconnected, fairly smooth micron-sized carbon ligaments that define a continuous macroporous network. This pore morphology is consistent with earlier reports of conventional CAs [6]. The macroporous network results in a relatively low surface area of 26 m^2/g. This relatively low surface area is due to the lack of microporosity in the DIW-CA (Table 1) which provided significant surface area for the pre-activated CA in previous reports. After activation resulting in 60% mass loss, the surface area for the DIW-ACA increases to over 1800 m^2/g which is on the same order of that observed in other activated CAs [6]. Figure 3d reveals that after activation, the surface of the carbon particles is much rougher, and a much finer network structure emerges after the CO_2 activation.

Table 1: Physical properties of the 3D printed carbon aerogels

Sample	**Density (g/cm^3)**	**BET Surface Area (m^2/g)**	**Total Pore Volume (cm^3/g)**	**Micropore Pore Volume (cm^3/g)**	**Electrical Conductivity (S/m)**
DIW-CA	0.47	26.5	0.083	0.004	995
DIW-ACA	0.24	1894	0.746	0.638	180

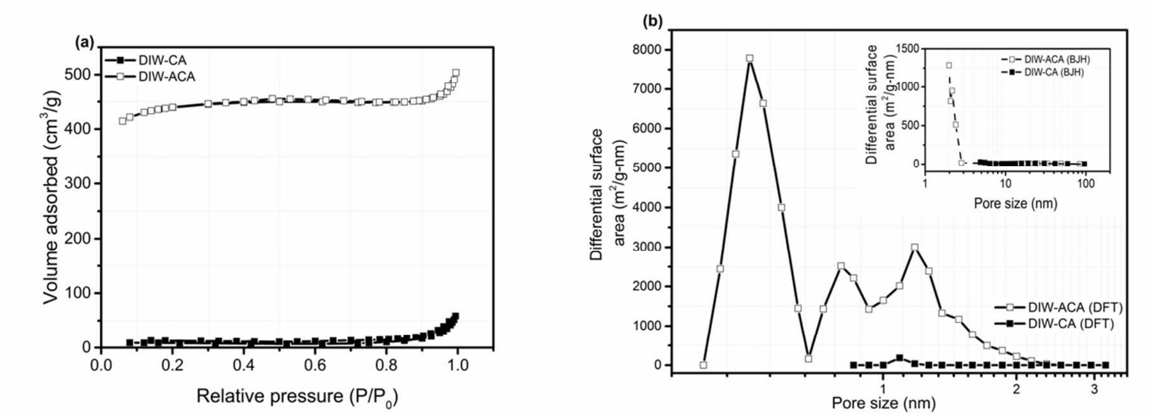

Figure 4: (a) Nitrogen adsorption/desorption isotherms and (b) pore size distribution of DIW-CA and DIW-ACA.

The microporous nature of the DIW-ACA is especially clear when examining the type II nitrogen adsorption-desorption isotherms in Fig. 4a with large absorbed volumes at low relative pressures. Other physical properties of the DIW-CA and DIW-ACA are summarized in Table 1. The two orders of magnitude increase in micropore volume suggests that a significant portion of this additional surface area is due to the formation of micropores. The pore size distributions as determined by Barrett-Joyner-Halenda (BJH) and density functional theory (DFT) methods support this conclusion (Fig. 4b). DIW-ACA, unlike the DIW-CA, contained significant microporosity with a sharp increase in surface area at low pore sizes. The BJH method does not accurately determine pore size in the micropore regime (<2 nm) so further analysis via DFT method was performed. Micropore analysis confirmed that nearly all the surface area in the DIW-ACA was due to newly formed pores less than 3 nm in diameter. These micropores give the DIW-ACA surface areas 3-50 times higher than other 3D-printed carbon-based aerogels [12, 15, 16]. Together with good electrical conductivity (180 S/m), the DIW-ACA should be a promising electrode material for water purification, electrocatalysis, and energy storage.

The electrochemical performances of the Bulk-CA (i.e. CA without architected pores), DIW-CA, and DIW-ACA (1.8 mm thick) electrodes, were evaluated in a three-electrode electrolytic cell in 3M KOH aqueous solution. The cyclic voltammetry (CV) curves and the galvanostatic charge discharge (GCD) curves are presented in Fig. 5a-f.

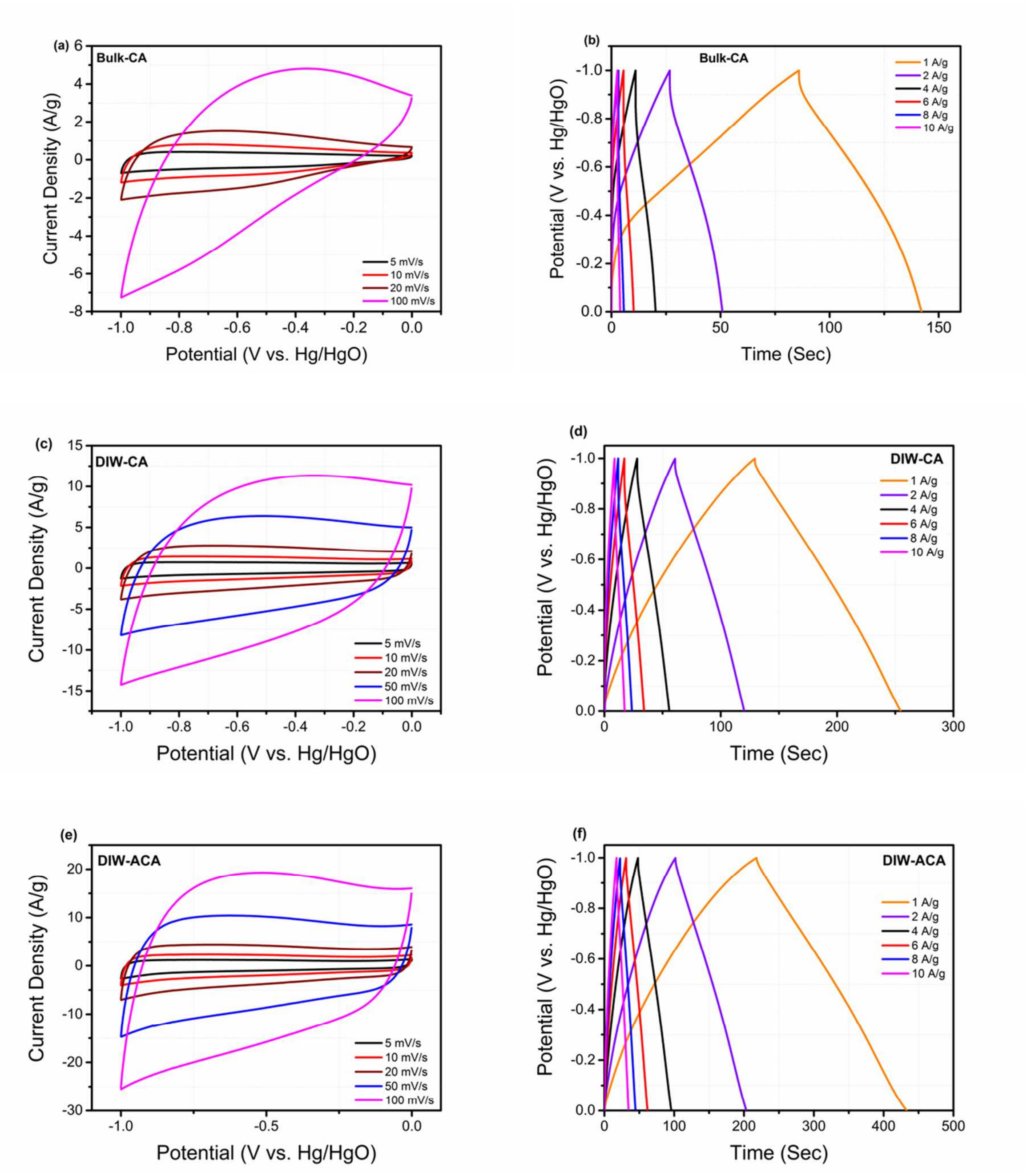

Figure 5: Electrochemical performance of Bulk-CA, DIW-CA and DIW-ACA. (a, c and e) Cyclic voltammograms collected as a function of scan rate. (b, d and f) Galvanostatic charge and discharge profiles collected at different current densities.

The CV and GCD curves provide good illustrations of how the pore architecture and surface area impact the capacitive performance of aerogels. The Bulk-CA represents the case without architected porosity, limited to native, random pores of 1 μm and below. Due to the limitations that this pore structure puts on mass transport within thick Bulk-CA, the CV curves exhibit gross distortions from the ideal rectangular shape at higher scan rates and the GCD curves deviate sharply from the ideal symmetric triangle (Fig. 5a and b). By contrast, simply adding architected macropores, DIW-CA, produces CV curves with a much more rectangular and triangular shape for the CV and GCD curves, respectively. Finally, adding surface area to the electrode with architected micropores, DIW-ACA, yields CV and GCD curves that are even closer to the ideal shapes indicative of excellent capacitive performance. In particular, DIW-ACA electrodes exhibit considerably enhanced gravimetric capacitance compared with the DIW-CA electrodes. This enhancement in capacitance can be ascribed to the substantially increased specific surface area after thermal activation, which provides more accessible surface area for the electrolyte ions for diffusion. It is presumed that all the surface area detected by nitrogen porosimetry (>1800 m^2/g) in the DIW-ACA is not electrochemically active as there is only factor of two increase in capacitance between the DIW-ACA and DIW-CA while the surface area increases by two orders of magnitude. Efforts to increase the electrochemically active area is being pursued in a separate study. The small *iR* drop in the GCD curves indicate the small internal resistance of the electrodes. DIW-ACA electrodes with a longer discharge time than DIW-CA at all current densities also reflect the increased specific capacitance of activated carbon aerogels [22].

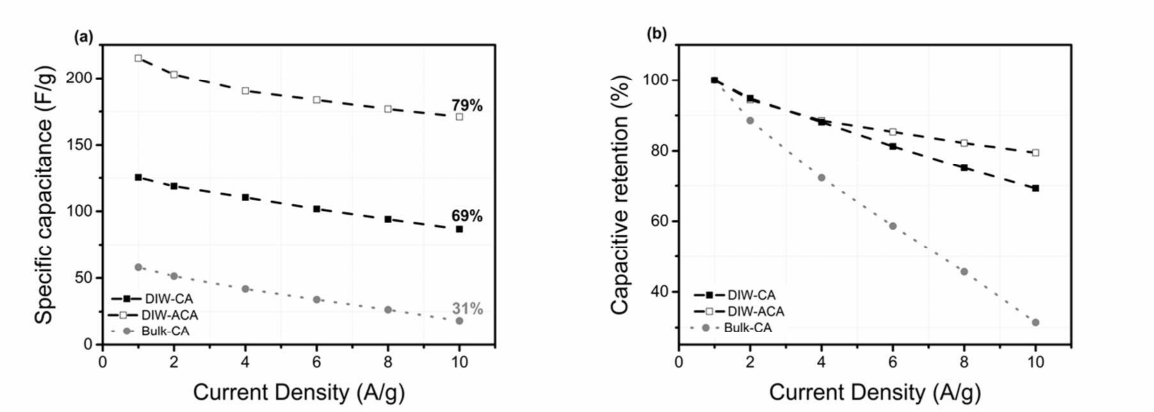

Figure 6: (a) Specific capacitance and (b) capacitive retention of DIW-CA, DIW-ACA and bulk-CA.

The gravimetric capacitance and volumetric capacitance for each sample is calculated from the GCD curves collected at different current densities and are summarized in Fig. 6a and Fig. S1. Comparing the DIW-CA with Bulk-CA (bulk discs prepared and processed in the same manner as DIW-CA) the specific capacitance of the DIW-CA (125 F/g at 1 A/g, 88 F/cm^3 at 1 A/g) is nearly twice that of the Bulk-CA-ink (57 F/g at 1 A/g, 58 F/cm^3 at 1 A/g). As the only difference between the Bulk-CA and DIW-CA is the 3D printed macroporosity (e.g. surface area, conductivity, pore size, etc. are equal), this result suggests that the macropores of the DIW-CA significantly improve ion accessibility [17, 23]. Comparing the DIW-CA and DIW-ACA we see a further increase in capacitance. The DIW-ACA exhibited a high gravimetric capacitance of 215 F/g (103 F/cm^3) at a current density of 1 A/g, which is almost twice as much as that of DIW-CA (125 F/g at 1 A/g, 88 F/cm^3 at 1 A/g). This enhancement in capacitance is attributed to the increased surface area after thermal activation. The gravimetric capacitance of DIW-ACA exceeds the previously reported GO-GNP composite aerogel exhibiting 70 F/g at low current densities [17]. As the current density is increased, efficient electron transport and ion diffusion are necessary for charge build up and the resistance of the sample plays a vital role in the rate capability of the electrode. Both DIW-CA and DIW-ACA also have good capacitive retention of 69% and 79% (Fig. 6b) respectively at higher current density (10 A/g), which is more than twice that of the Bulk-CA. After activation, the gravimetric capacitance has been increased, and the rate capability has also been increased, suggesting that the increased porosity after activation improves the ion accessibility. The improved rate capability observed with the DIW-CA and DIW-ACA confirm the importance of using engineered macropores in aerogel electrodes for enhancing charged species transport.

3D printing enables an ordered macropore electrode architecture which facilitates mass transfer by reducing the ion diffusion resistance. To understand the correlation between macroporosity and capacitive performance, electrodes were printed with different nozzle diameters (*d*) (400, 200 and 100 μm) with center-to-center rod spacing (*L*) of 800 μm and the height of the printed electrodes were kept constant to 1.5 mm. DIW-CA electrodes with varied spacing-to-diameter ratio (*L/d*) of 2 (800/400), 4 (800/200) and 8 (800/100) were synthesized in a similar fashion and addressed as DIW-CA-2, DIW-CA-4, and DIW-CA-8, respectively. The electrochemical performance of these samples along with their CV and GCD curves are presented in Fig. 7a-f.

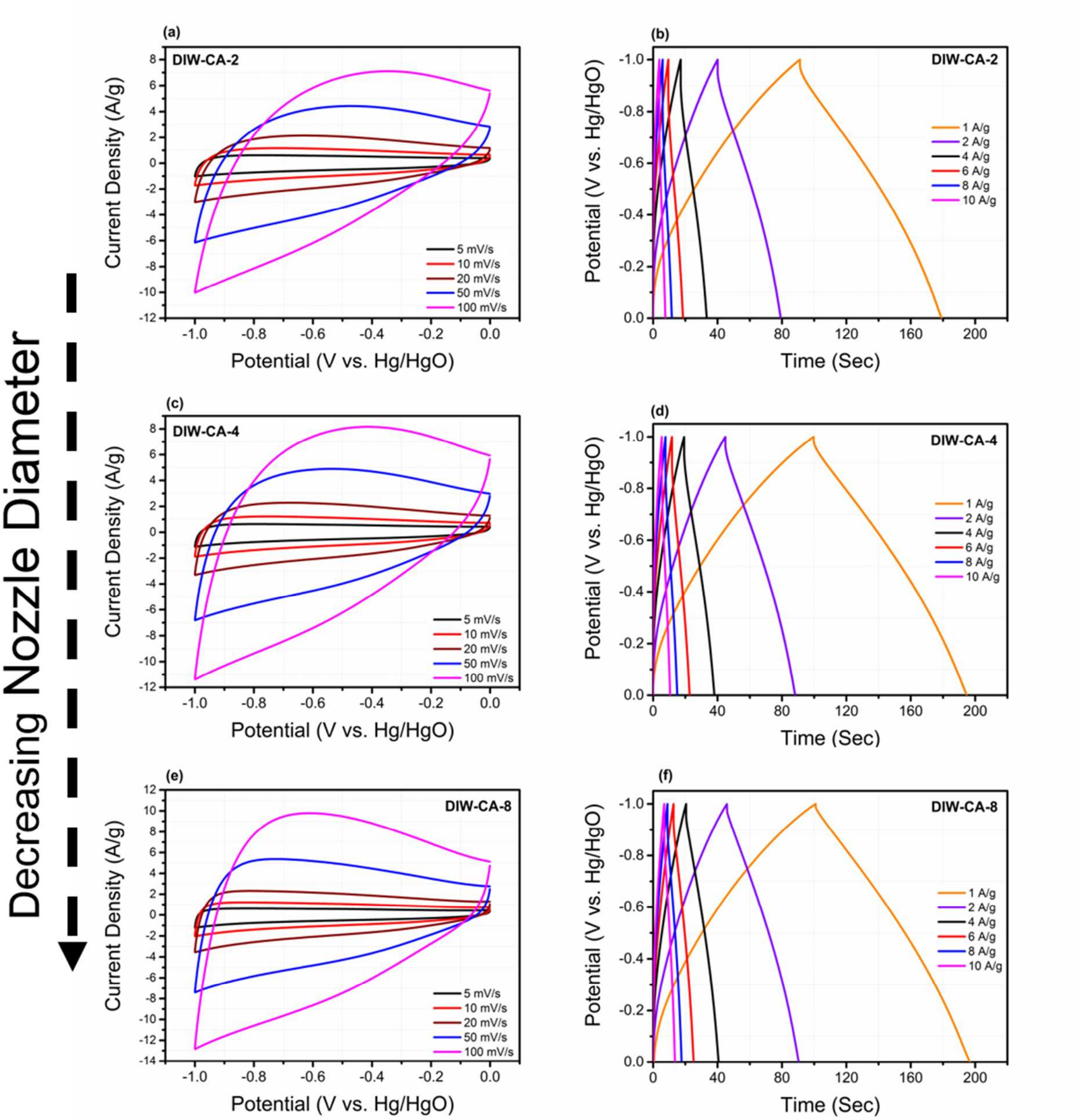

Figure 7: (a-c) CV curves and (d-f) GCD curves for DIW-CA-2, DIW-CA-4, and DIW-CA-8, respectively.

As can been seen in Fig. 7, when the nozzle diameter decreases from 400 μm to 100 μm, the CV curves (Fig. 7a, c, e) collected at higher scan rate (100 mV/s) have larger hysteresis loops which suggests better charge transfer through the ligaments as the ion diffusion length decreases with decreasing the nozzle diameter. The GCD curves (Fig. 7b, d, f) show an increase in discharge time as the nozzle diameter is decreased from 400 μm to 100 μm at a current density of 1 A/g. Although the DIW-CA electrodes with 200 μm and 400 μm show comparable gravimetric and volumetric capacitance under small current densities, their capacitive differences became more obvious when the current is increased. This data are summarized in Fig. 8 and Fig. S2.

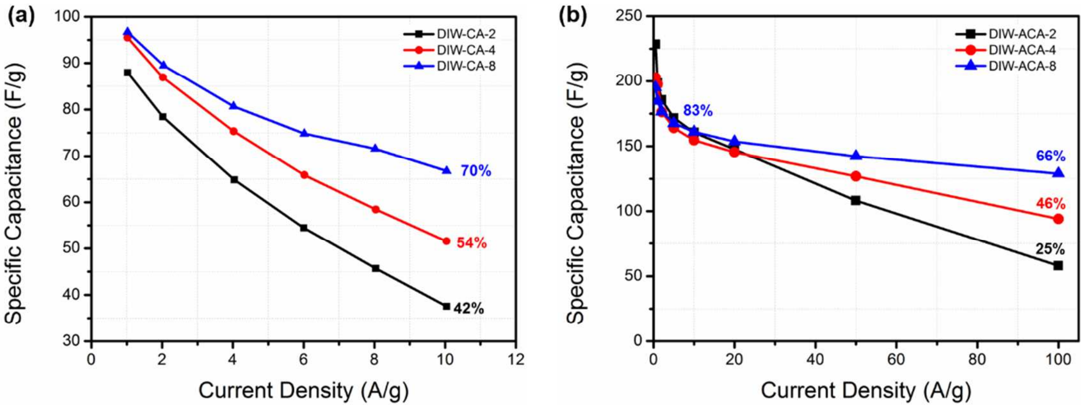

Figure 8: Gravimetric capacitance of the (a) DIW-CA-2. DIW-CA-4, DIW-CA-8 and (b) DIW-ACA-2, DIW-ACA-4 and DIW-ACA-8 electrodes obtained at different current densities.

Although these three DIW-CA samples have similar gravimetric capacitances at low current density of 1 A/g, the effect of varying nozzle diameters becomes more significant at the higher current density of 10 A/g. The capacitive retention of the sample printed with 400 μm nozzle is only 42% and is improved to 70% when printed with 100 μm nozzle diameter. By varying the filament diameter of the printed electrode, the ion diffusion length is varied and affects the electrochemical performance of these electrodes. After the samples are activated, the DIW-ACA electrodes display more rectangular shapes and increased discharge times, suggesting improved ion diffusion and increased specific surface areas (Fig. S3). As observed Fig. 8b and Fig. S4, both the specific capacitances, volumetric capacitance, and the rate capabilities of DIW-ACA electrodes have further increased compared with the DIW-CA electrodes with the same spacing-to-diameter ratios. For example, the DIW-ACA-8 electrode shows more than twice the specific capacitance of the DIW-CA-8 electrode at 1 A/g. These differences become even more distinct at higher current densities. The DIW-ACA-8 can retain 83% of its capacitance at 10 A/g (compared to 70% for DIW-CA-8) and even 66 % at 100 A/g.

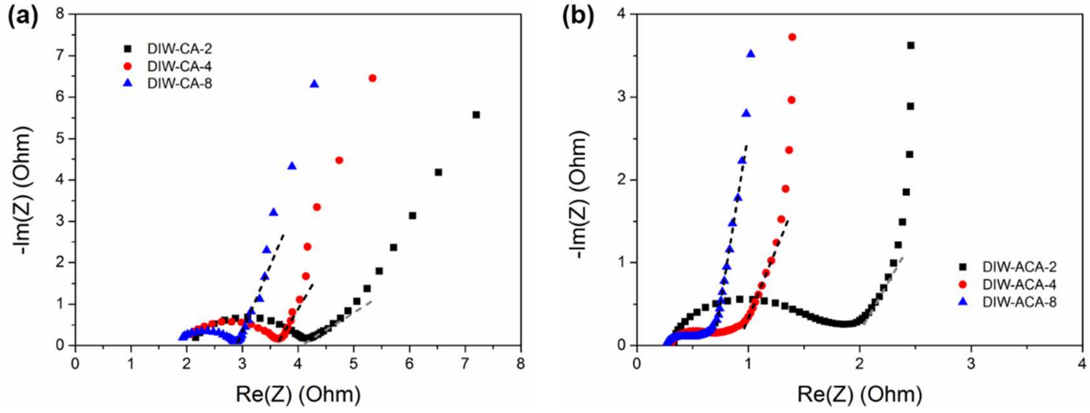

Figure 9: Electrochemical impedance spectroscopy of (a) DIW-CA-2. DIW-CA-4, DIW-CA-8 and (b) DIW-ACA-2, DIW-ACA-4 and DIW-ACA-8.

Electrochemical impedance spectroscopy (EIS) was used to gain more insight into the excellent performance of DIW electrodes. As shown in Figure 9a, all the DIW-CAs electrodes have similar equivalent series resistance (ESR), which are 2.16, 2.07 and 1.93 ohm for DIW-CA-2, DIW-CA-4 and DIW-CA-8, respectively. The knee frequency is the frequency at which pure capacitance behavior can be obtained and most of its stored energy is accessible at frequencies below this frequency. The knee frequencies of DIW-CA-2, DIW-CA-4 and DIW-CA-8 are 3.85, 18.1 and 25.9 Hz, respectively. The higher the knee frequency represents the less the time is needed for DIW-CA-8 to finish the surface charge accumulation, which is favorable for fast charging and achieving a good rate performance. For the DIW-ACAs electrodes, the ESRs of DIW-ACA-2, DIW-ACA-4 and DIW-ACA-8 are 0.47, 0.31 and 0.26 ohm, respectively (Figure 9b). The decreased ESRs of DIW-ACAs electrodes are due to the increased porosity after activation, which is consistent with the previous reports [24, 25]. The knee frequencies are 5.48, 56.69 and 90.49 Hz for DIW-ACA-2, DIW-ACA-4 and DIW-ACA-8, respectively. Notably, the considerably higher knee frequencies of the DIW-ACA compared to the DIW-CA electrodes suggests less time is required for the surface charge accumulation at the interface. This improved performance is believed to be due to the improved ion diffusion as a result of the increased porosity after activation and is directly evidenced by the better rate capability.

Previous research has shown that the linear section in the intermediate frequencies (the Warburg region) is associated with ion diffusion resistivity [26, 27]. A higher slope in the Warburg region corresponds to the lower diffusion resistivity. As shown in Figure 9a and 9b, in general the DIW electrodes with higher spacing-to-diameter ratios exhibit lower ion diffusion resistivity compared with the electrode materials with smaller spacing-to-diameter ratios. Importantly, the DIW-ACAs electrodes show improved ion diffusion capability compared to the DIW-CAs at the same spacing-to-diameter ratio, again confirming the additional benefit of activation process.

Conclusion

In summary, a method to additively manufacture traditional resorcinol-formaldehyde organic aerogels using direct ink writing technology has been demonstrated in this work. The 3D-printed organic aerogel was converted to a carbon aerogel which successfully maintained the engineered microarchitecture of the original organic aerogel print. A critical step for successful 3D printing of the carbon aerogels was the development of a thixotropic, printable sol-gel ink. It was determined that several key features of the microstructure (both macro- and microporosity) can have a profound impact on the electrode performance. Decreasing the minimum feature size from 400 µm to 100 µm also had a significant effect of improving the capacitive retention from 42% to 70%, respectively. Lastly, by tuning the surface area of the 3D printed CAs through thermal activation, the specific capacitance of these electrodes was doubled compared to the unactivated electrodes. This resulted in electrodes that exhibited 215 F/g at 1 A/g and a 83% capacitive retention when the current density is increased 10-fold to 10 A/g. Thus, with the possibility to 3D print traditional sol-gel-derived carbon aerogels with engineered macro-pore architecture, future studies will look at the impact of architected porous carbon on other technologies, such as batteries, electrocatalysis and separations.

Acknowledgements

This work was done under the auspices of the U.S. Department of Energy under Contract DE-AC52-07NA27344, through LDRD award 16-ERD-051.

Fabrication of the 3D printed electrodes

Resorcinol (R) and formaldehyde solution (F) (37 wt%) purchased from Sigma Aldrich were used to prepare the organic aerogels. Predetermined amounts of formaldehyde solution (1.7 g), DI water (1.5 g) was mixed with 6 wt% of hydroxypropyl methyl cellulose (purchased from DOW chemicals). The mixture is sonicated in a temperature-controlled bath for 24h. To this mixture, 1.23g of R and 44 μL of glacial acetic acid. To further tailor the ink to be thixotropic, 9wt% of Carbosil-EH5 fumed silica, was added and mixed in the Thinky mixture at 2000 rpm for 5 minutes. The as-prepared ink is loaded into a 3ml syringe barrel (EFD) and centrifuged for a minute at 4500 rpm to remove air bubbles, after which the ink is extruded through a micro nozzle (400 μm diameter) to pattern 3D structures on a glass substrate. For direct ink writing, the syringe was attached by a luer-lock to a smooth-flow tapered nozzle whose inner diameter(d) is 400 μm. The ink was then extruded by means of an air powered fluid dispenser (Ultimus V, EFD) which provides an appropriate pressure (in the range of 12-15 psi) for writing and the writing speed was kept at 3 mm/sec for all the 3D printed structures. Simple cubic lattices with multiple orthogonal layers of parallel cylindrical rods were printed alternately. The diameter of the cylindrical rods equals the diameter of nozzle (d) and the center-to-center rod spacing (L) was varied depending on the type of electrode. The height of the electrodes was varied from 1 mm to 3 mm and the layers were stacked on the structure such that each layer has a z spacing of 60% the diameter of the nozzle diameter. To avoid cracking or drying due to evaporation of water, soon after printing, the 3D printed structures are immersed in a jar containing solvent (iso-octane) and cured in an oven at 80°C for 72 h to form organic aerogels.

Carbonization and activation of aerogels

This process involves carbonizing the super-critically dried RF gels to form carbon aerogels (CAs). The aerogels were subjected to a heat treatment process where the samples were heated in a tube furnace under nitrogen atmosphere at 1050°C for 3h with a heating and cooling rate of 2°C/min. The carbonized 3D printed graphene based CAs were then etched with hydrofluoric acid to remove fumed silica. The etched parts were again subjected to a three-day solvent (acetone) exchange followed by super critical drying. Activation was done thermally, according to a previous study [6]. This process involves the use of the Boudouard reaction, CO_2 reacting to carbon at 950°C to evolve CO, to controllably etch small pores in the CA. [28-31] In this case, the CA was thermally activated until a 60% mass loss of the sample was obtained. The DIW-ACA electrodes weighed ca. 3 mg.

Characterization

Nitrogen Porosimetry. Textural properties were determined by Brunauer-Emmett-Teller (BET) and Barrett-Joyner-Halenda (BJH) methods using an ASAP 2020 Surface Area Analyzer (Micromeritics Instrument Corporation) via nitrogen porosimetry [32, 33]. Samples of approximately 0.1 g were heated to 423 K under vacuum (10^{-3} Pa) for at least 24 hours to remove all adsorbed species. Scanning electron micrographs in Fig. 2 was obtained with a JEOL7401-F SEM at a 5kV accelerating voltage.

The electrochemical measurements were carried out using electrochemical workstation (CHI 660D and EC-Lab SP-300) in a three-electrode electrolytic cell under 3M KOH aqueous solution. The working electrodes were prepared by pressing carbon aerogels in between two pieces of nickel foams. A piece of carbon foil and Hg/HgO electrode were working as counter electrode and reference electrode, respectively.

Calculation

Gravimetric capacitance (C_g) of single electrodes are calculated based on the galvanostatic charging and discharging curves using the following equation. [34]

$$C_g = \frac{I \times t}{\Delta U \times m} \quad \text{(Equation 1)}$$

Where C_g is the gravimetric capacitance (F g^{-1}), ΔU is the potential window (V), I is the discharge current (A), t is the discharge time (s), and m is the mass loading of the materials on the electrodes (g).

Volumetric capacitance (C_v) of single electrodes are calculated based on the galvanostatic charging and discharging curves using the following equation.

$$C_v = \frac{I \times t}{\Delta U \times V} \quad \text{(Equation 2)}$$

Where C_v is the volumetric capacitance (F cm^{-3}), ΔU is the potential window (V), I is the discharge current (A), t is the discharge time (s), and V is the volume of the electrodes (cm^3).

References

[1] Pekala RW., Alviso CT.. Carbon Aerogels and Xerogels. *MRS Proc.*, 1992, **270**, 63.
[2] Moreno-Castilla C., Maldonado-Hódar FJ. *Carbon*, 2005, **43**, 455.
[3] Zhang S., Wang J., Shen J., Deng Z., Lai Z., Zhou B., Attia S., and Chen L.. *Nanostruct. Mater.*, 1999, **11**, 375.

[4] Biener J., Stadermann M., Suss M., Worsley MA., Biener MM., Rose KA.. and Baumann F.. *Energy Environ. Sci.*, 2011, **4**,656.

[5] Tamon H., Ishizaka H., Mikami M., Okazaki M.. *Carbon*, 1997, **35**, 791.

[6] Baumann TF., Worsley MA., Han TY-J., Satcher JH.. *J. Non-Cryst. Solids*, 2008, **354**, 3513.

[7] Kabbour H., Baumann TF., Satcher JH., Saulnier A., Ahn CC.. *Chem. Mater.*. 2006. **18**. 6085.

[8] Suss ME., Baumann TF., Bourcier WL., Spadaccini CM., Rose KA., Santiago JG., and Stadermann. M.. *Energy Environ. Sci.*, 2012, **5**, 9511.

[9] Zhai T., Lu X., Wang H., Wang G., Mathis T., Liu T., Li C., Tong Y., and Li Y.. *Nano Lett.*, 2015, **15**, 3189.

[10] Zhu C., Liu T., Qian F., Chen W., Chandrasekaran S., Yao B., Song Y., Duoss E. Kuntz J., Spadaccini C., Worsley M., and Li Y.. *Nano Today*, 2017, **15**, 107.

[11] Liu T., Zhu C., Kou T., Worsley MA., Qian F., Condes C., Duoss E., Spadaccini C., Li Y.. *ChemNanoMat*, 2016, **2**, 635.

[12] Zhu C., Han TY-J., Duoss EB., Golobic AM., Kuntz JD., Spadaccini CM., and Worsley M.. *Nat. Commun.*, 2015, **6**, 6962.

[13] Bauer J., Schroer A., Schwaiger R., Kraft O.. *Nat. Mater.*, 2016, **15**, 438.

[14] Kim JH., Chang WS., Kim D., Yang JR, Han JT, Lee G-W et al. 3D printing of reduced graphene oxide nanowires. *Adv. Mater.*, 2015, **27**, 157.

[15] Lin Y., Liu F., Casano G., Bhavsar R., Kinloch IA., and Derby B.. *Adv. Mater.*, 2016, **28**, 7993.

[16] Zhang Q., Zhang F., Medarametla SP., Li H., Zhou C., and Lin D.. *Small*, 2016, **12**, 1702.

[17] Zhu C., Liu T., Qian F., Han TY-J, Duoss EB., Kuntz JD., Spadaccini C., Worsley M., and Li Y.. *Nano Lett.*, 2016, **16**, 3448.

[18] Tang X., Zhou H., Cai Z., Cheng D., He P., Xie P., Zhang D., and Fan T. *ACS Nano*, 2018, **12**, 3502.

[19] Ge Y., Zhang T., Zhou B., Wang H., Zhang Z., Shen J., and Du A.. *J. Mater. Res.*, 2018, **92**, 1.

[20] Guo F., Jiang Y., Xu Z., Xiao Y., Fang B., Liu Y., Gao W.,Zhao P., Wang H., and Gao C.. *Nat. Commun.*, 2018, **9**, 661.

[21] Jiang Y., Xu Z., Huang T., Liu Y., Guo F., Xi J., Gao W., and Gao C.. *Adv. Funct. Mater.*, 2018, **306**, 1707024.

[22] Fang B., Wei YZ., Maruyama K., and Kumagai M. *J. Appl. Electrochem.*, 2005, **35**, 229.

[23] Merrill MD., Montalvo E., Campbell PG., Wang YM., Stadermann M., Baumann TF., Biener, J., and Worsley M.. *RSC Adv.*, 2014, **4**, 42942.

[24] Zhang, F., Liu, T., Hou, G., Kou, T., Yue, L., Guan, R., and Li, Y.. *Nano Res.*, 2018, **9**, 2875.

[25] Abouelamaiem, DI., He, G., Neville, TP., Patel, D., Ji, S., Wang, R., Parkin, IP., Jorge, AB., Titirici, M-M., Shearing, and PR, Brett, D.. *Electrochimica Acta*, 2018, DOI: https://doi.org/10.1016/j.electacta.2018.07.190.

[26] Wu, X., Guo, Y., Su, J., Xiong, J., Zhang, Y., and Wan, L.. *Adv. Energy Mater.*, 2013, **3**, 1155.

[27] Song, Y., Liu, T., Yao, B., Li, M., Kou, T., Huang, Z., Feng, D., Wang, F., Tong, Y., Liu, X., and Li Y.. *ACS Energy Lett.,* 2017, **2**, 1752-1759.

[28] Hanzawa Y., Kaneko K., Pekala R.W., Dresselhaus M.S., *Langmuir,* 1996, **12**, 6167.

[29] Feaver A., Cao G., *Carbon*, 2006, **44**, 590.

[30] Saliger R., Fischer U., Herta C., Fricke J., *J. Non-Cryst. Solids*, 1998, **225**, 81.

[31] Lin C., Ritter J.A., *Carbon*, 2000, **38**, 849.

[32] Gregg S. J., and Sing K. S. W.. *Adsorption, Surface Area and Porosity*.: Academic Press; 1982.

[33] Rouquerol F., Rouquerol J., Sing K.W.S.. Adsorption by Powders and Porous Solids. Principles, Methodology and Applications, Academic, 1999.

[34] Yang, P., Mai, W. *Nano Energy,* 2014, ***8***, 274-290.

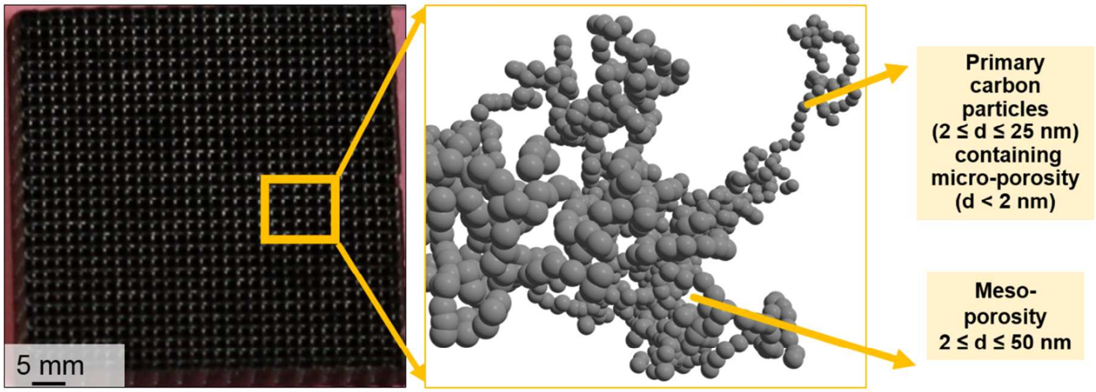
5 mm
Primary carbon particles (2 ≤ d ≤ 25 nm) containing micro-porosity (d < 2 nm)
Meso-porosity 2 ≤ d ≤ 50 nm